

Site-Selective Preparation and Multistate Readout of Molecules in Optical Tweezers

Lewis R. B. Picard^{1,2,3,‡}, Gabriel E. Patenotte^{1,2,3,‡}, Annie J. Park,^{1,2,3,‡,*}
Samuel F. Gebretsadkan,^{1,2,3} and Kang-Kuen Ni^{1,2,3,†}

¹ Department of Physics, Harvard University, Cambridge, Massachusetts 02138, USA

² Department of Chemistry and Chemical Biology, Harvard University, Cambridge, Massachusetts 02138, USA

³ Harvard-MIT Center for Ultracold Atoms, Cambridge, Massachusetts 02138, USA

(Received 30 January 2024; revised 1 April 2024; accepted 5 April 2024; published 28 May 2024)

Polar molecules are a quantum resource with rich internal structure that can be coherently controlled. The structure, however, also makes the state preparation and measurement (SPAM) of molecules challenging. We advance the SPAM of individual molecules assembled from constituent atoms trapped in optical-tweezer arrays. Sites without NaCs molecules are eliminated using high-fidelity Cs atom detection, increasing the peak molecule filling fraction of the array threefold. We site-selectively initialize the array in a rotational qubit subspace that is insensitive to differential ac Stark shifts from the optical tweezer. Lastly, we detect multiple rotational states per experimental cycle by imaging atoms after sequential state-selective dissociations. These demonstrations extend the SPAM capabilities of molecules for quantum information, simulation, and metrology.

DOI: 10.1103/PRXQuantum.5.020344

I. INTRODUCTION

Polar molecules feature a rich internal structure with tunable long-range dipolar interactions, making them a resource for a wide range of quantum science applications. Coherent control of internal states [1–7] is key to many recent advances. The dipole-dipole interaction has been used to realize a spin Hamiltonian [8], the site-resolved correlations of which have been measured in an optical lattice [9], and to produce Bell states in optical tweezers [10,11] for dipolar quantum gates [12]. Control over nuclear spins has transferred their entanglement from reactants to products in chemical reactions [13]. In the search for the electron electric dipole moment, internal states have been polarized to generate large laboratory-frame electric fields and used to evaluate systematic errors [14–16]. Many applications require further advances in state preparation and measurement (SPAM), which remains an outstanding challenge due to the dense electronic and

vibrational structure that complicates molecule production and detection.

Nondestructive detection using fluorescence from optical-cycling transitions has become an indispensable technique in atomic physics. Real-time detection of individual atoms enables the rearrangement of occupied traps to produce a densely filled array [17–19], as well as the selective readout of their internal states [20,21]. Both capabilities are crucial for studying many-body interactions and executing large quantum circuits [22–25]. For molecules, a subset [26,27] do possess optical-cycling transitions, enabling advances in their laser cooling [28,29], trapping [30–32], and rearrangement [10]. Other molecules can be produced by the coherent association of their constituent atoms [33–45], with the advantage that cold-atom temperatures are preserved in the molecule creation process. However, optical-cycling transitions for fluorescence or absorption imaging are generally not available. In general, the population of a specific state of associated molecules is detected through the adiabatic dissociation of the constituent atoms, which are then separated and imaged. To make use of the inherent multilevel structure of molecules, three capabilities for the molecule SPAM toolbox are highly desirable: rearrangement while maintaining low temperature, site-resolved state preparation, and resolved readout of multiple internal states. The first capability would allow for the production of deterministically filled arrays of molecules. The latter two would facilitate experiments using the many long-lived rotational states as a qudit

*Corresponding author: jpark4@fas.harvard.edu

†Corresponding author: ni@chemistry.harvard.edu

‡These authors contributed equally to this work.

system or multilevel quantum simulator [46,47]. Various proposals have been put forward for molecule readout via a controlled interaction between a ground-state molecule and an ancilla atom or optical cavity [48–54]. However, these methods require the introduction of a new coherently controlled interaction between the molecule and the detection ancilla, which requires more experimental overhead to implement.

Here, we demonstrate an immediately-applicable method for the removal of defects in a molecular array and sequential state-selective detection. Our proposed scheme uses fluorescence imaging of the constituent atoms of NaCs, as shown in Fig. 1. Unassociated Cs atoms are detected immediately following molecule formation to infer which sites contain molecules. We rearrange those sites and increase the local filling probability at the edge of the array threefold. We also use the atom signal for the detection of the two molecular states in the ground $|0\rangle$ and first excited $|1\rangle$ rotational levels that form our computational basis. In a single experimental cycle, molecules are sequentially dissociated from each state and the resulting Cs atoms are detected. Lastly, we demonstrate the ability to initialize an array of molecules in an arbitrary pattern of the computational basis states, using global microwave pulses in combination with an auxiliary rotational state outside the computational basis for site-selective shelving of molecules.

This work is organized as follows. In Sec. II, we detail the implementation of Cs imaging at the high magnetic field conditions in which molecules are prepared. In Secs. III and IV, we demonstrate molecule rearrangement and sequential imaging of multiple rotational states. In Sec. V, we demonstrate site-selective rotational excitations. We conclude with suggested applications and improvements to the fidelities of these schemes in Sec. VI.

II. HIGH-FIELD ATOM IMAGING

Both the rearrangement of molecules and their sequential state-selective readout rely on the detection of atoms at or near the magnetic field at which molecules are assembled. Our preparation of NaCs in its rovibrational and electronic ground state has been detailed previously [55–57]. In summary, we prepare parallel 1×8 arrays of hyperfine ground-state Na and Cs atoms close to the three-dimensional motional ground state of their respective 616-nm and 1064-nm optical tweezers. Na atoms are then adiabatically transferred into the 1064-nm array, such that each 1064-nm tweezer contains, ideally, individual Na and Cs atoms in their motional and hyperfine ground states. Atom pairs are magnetoassociated into a weakly bound molecule via a Feshbach resonance at 864 G and transferred to a rovibrational and electronic ground hyperfine state ($|m_{I_{\text{Na}}} = 3/2, m_{I_{\text{Cs}}} = 5/2\rangle$) via a detuned Raman process [55,56].

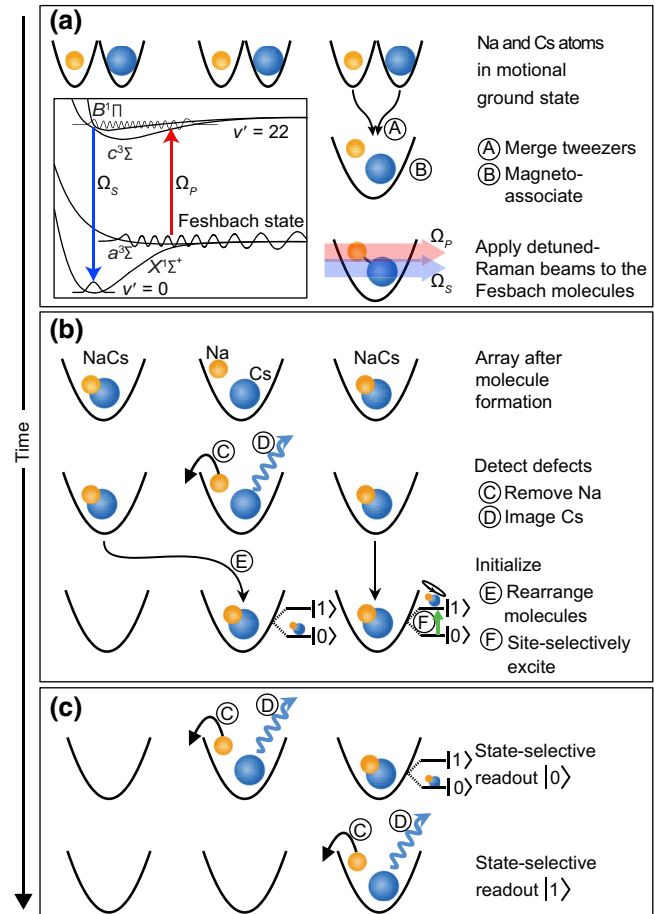


FIG. 1. An overview of an experimental sequence with novel SPAM techniques showing the (a) molecule production, (b) rearrangement and state initialization, and (c) state-selective readout of NaCs molecules. For details on the coherent association and transfer of atoms to the molecular ground state, see Appendix B. The detection of unassociated Cs atoms (C),(D) enables the rearrangement of molecules to more densely filled array (E). An auxiliary rotational state is used for site-selective initialization (F) in a noise-insensitive computational basis of two rotational states. In addition, the detection of atoms from state-selectively dissociated molecules is harnessed for multistate readout of the computational basis.

To detect the unassociated atoms, we extend the low-field state-selective fluorescence imaging of Cs atoms in optical tweezers [58,59] to a high magnetic field, similar to the high-field absorption detection of a cloud of potassium atoms [60]. In principle, one could also image Na atoms on the equivalent stretched D_2 transition. We opt to image Cs atoms due to the 5 times stronger polarizability of Cs in the 1064-nm tweezers, which reduces the tweezer intensity required to trap atoms that are heated during imaging. The magnetic field decouples the total angular momentum F of the excited fine-structure levels, such that the quantum numbers $|m_I, m_J\rangle$ best describe the excited hyperfine states, where I is the

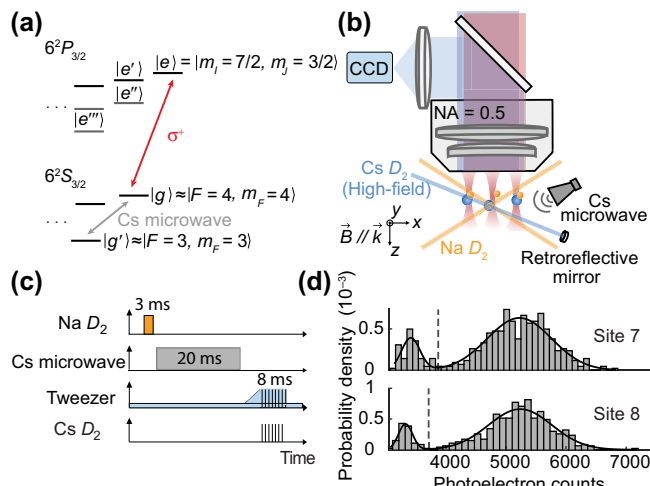


FIG. 2. State-selective detection of Cs at 864 G. (a) The simplified energy structure of Cs, showing the hyperfine state $|g'\rangle$ in which Cs atoms are initialized and the optical-cycling transition between $|g\rangle$ and $|e\rangle$ used for fluorescence imaging. (b) A schematic of the apparatus, depicting the beams used for the ejection of sodium atoms and for driving the Cs optical-cycling transition. The Cs hyperfine transition is driven by a microwave horn antenna. Fluorescence is collected by a 0.55-numerical-aperture (NA) objective and CCD camera. (c) The timing diagram for the imaging process, including Na ejection via near-resonant D_2 light, Cs microwave transfer from $|g'\rangle$ to $|g\rangle$, and optical cycling. The tweezer and imaging light are pulsed out of phase since $|e\rangle$ is antitrapped. (d) Histograms of the collected fluorescence from Cs atoms.

nuclear spin ($I_{\text{Cs}} = 7/2$), J is the total electronic spin, and m denotes their projections along the magnetic field axis. Detection is performed by exciting from $|g'\rangle \approx 6^2S_{1/2} |F=3, m_F=3\rangle$ to $|g\rangle \equiv 6^2S_{1/2} |F=4, m_F=4\rangle$ and optically cycling on the stretched D_2 transition $|g\rangle$ to $|e\rangle \equiv 6^2P_{3/2} |m_I=7/2, m_J=3/2\rangle$. The optical-cycling transition is depicted in Fig. 2(a), along with nearby states that can have nonzero coupling to non- σ^+ components of the imaging light. An advantage of the high-field regime is significant detuning protection against populating these off-resonant states, the composition and energy of which are provided in Appendix A.

Following molecule creation or dissociation, Cs atoms are initialized in $|g'\rangle_{\text{Cs}}$ and may share their optical tweezer with Na atoms in $|g'\rangle_{\text{Na}} \approx 3^2S_{1/2} |F=1, m_F=1\rangle$. We must eject Na atoms before exciting Cs to $|g\rangle_{\text{Cs}}$ to avoid spin-changing inelastic collisions that occur when the atoms are not both in spin-stretched hyperfine states [43]. As shown in Fig. 2(b), which depicts the geometry of the apparatus, the Na atoms are heated out of the trap by beams at the D_2 transition frequency that are originally used to produce the Na magneto-optical trap (MOT). The Cs atoms are then excited from $|g'\rangle$ to $|g\rangle$ using a microwave horn with negligible off-resonant coupling due

to a $h \times 250$ MHz detuning with the next nearest transition. Lastly, we optically cycle on the $|g\rangle$ to $|e\rangle$ transition using a small retroreflected imaging beam with a $1/e^2$ waist of approximately 1 mm, collecting fluorescence photons through a 0.55-NA objective onto a charge-coupled device (CCD) camera. The use of a small imaging beam helps suppress background noise due to light scattered from the surface of the glass cell into the objective. Polarization along the y axis is chosen to mitigate the π -polarized $|g\rangle$ to $|e\rangle \approx 6^2P_{3/2} |m_I=5/2, m_J=3/2\rangle$ transition, which is closest detuned by $h \times 67$ MHz. Crucially, none of the 589-nm Na D_2 light, the 852-nm Cs D_2 light, or the $h \times 11.34$ GHz microwave measurably affect the NaCs molecules.

The timing diagram of high-field imaging is shown in Fig. 2(c). We observe complete ejection of Na from the trap within 3 ms. For the microwave transition, instability in the magnetic field on the approximately 15 mG level limits the transfer efficiency given the available microwave Rabi frequency. To maximize efficiency in the presence of this noise, we use an adiabatic rapid passage pulse in which the frequency is linearly swept across a 400-kHz range about the resonance in 20 ms. As the imaging provides no cooling except for red-detuned Doppler cooling along the imaging beam axis, we increase the peak trap intensity to 1.25 MW/cm² to collect sufficient fluoresced photons before atom loss to resolve the presence of an atom over background noise. The optical-cycling transition is driven near resonantly to minimize the time that the molecules, the loss rate of which from $|0\rangle$ due to scattering of the trap light is 7 Hz/(MW/cm²), need to be held at high depth. Due to scattering, we observe a 5.6(8)% loss of molecules during high-field Cs imaging. We also strobe the imaging and tweezer light out of phase with a 10% and 70% duty cycle, respectively, at 500 kHz to prevent heating due to $|e\rangle$ being antitrapped [20,61].

The imaging fidelity is calculated from histograms like those shown in Fig. 2(d) using a standard method that is described in Appendix C. In order to analyze the imaging fidelity, we prepare Cs atoms in $|g'\rangle$ cotrapped with Na atoms at high magnetic field without undergoing Feshbach association. The fidelity of sodium ejection and subsequent Cs imaging is verified using the sequence shown in Fig. 2(c). By averaging the collected signal of the CCD camera for each site over many experimental cycles, we observe two Gaussian distributions: a “dark” peak corresponding to electronic read noise of the camera, and a “bright” peak corresponding to atom fluorescence. Based on histogram analysis, we report a 0.38(9)% false-positive rate and 0.089(2)% false-negative rate for Cs atoms prepared in $|g\rangle$. There is an additional false-negative rate of 0.149(8)% due to Raman processes induced by tweezer and imaging lights. Taking these factors into account, we achieve an overall imaging fidelity of 99.4(1)%. Due to imperfect microwave transfer and

state-preparation fidelity, the false-negative rate increases to 3.6(7)% for Cs atoms initialized in $|g'\rangle$, which is the case for molecule rearrangement and sequential imaging. Our simulation shows that the increased false-negative rate can be explained by the microwave transfer inefficiency due to the magnetic field instability of approximately 15 mG. The transfer efficiency can be improved by using more powerful amplifier or nonlinear amplitude and frequency ramps [62].

III. MOLECULE REARRANGEMENT

We use the high-field detection of Cs atoms to produce a dense array of molecules without increasing their motional energy. To infer which traps contain molecules, we use a combination of three atom images. After the loading and rearrangement of atomic arrays, we detect the initial Na and Cs occupations with fluorescence imaging. The atoms are then Raman sideband cooled to near their motional ground state and the arrays are adiabatically combined. As stated in Sec. II, Cs atoms are detected again at high-field following molecule production using previously determined thresholds. Molecules may only be found at sites in which both atoms were detected at low field in the first two images, because two atoms are needed to form a diatomic molecule, and where Cs was not detected at high field in the third image, because the molecules are dark to high-field Cs detection. Such cases correspond to 27% of the sites that will be preserved by the rearrangement algorithm.

Three relevant mechanisms can result in the preserved sites not containing ground-state molecules, which are depicted in Fig. 3(a). The first is when atom pairs that associate into Feshbach molecules are lost during detuned Raman transfer, which has a one-way transfer efficiency of 76(3)%, limited by a combination of inhomogeneous intensities of the Raman beams across the array, time variation of the intensities of the beams, and scattering from the intermediate state of the transfer [55,56]. The second is that Cs atoms may be lost between low-field and high-field detection, which falsely appears as molecule production. Cs can be lost during the merging of the two arrays (0.7(9)% or in spin-changing inelastic collisions with sodium in several milliseconds after merge (1(1)% if either atom is prepared in the wrong hyperfine state. A third concern is that Cs atoms may not be detected due to imperfect microwave transfer and state preparation, as described in Sec. II. We estimate based on these mechanisms that 71(3)% of the preserved sites, or 19(2)% of all sites, contain a ground-state molecule.

The rearrangement of molecules proceeds as follows. Optical tweezers for sites that are not preserved are turned off. Starting sequentially from the rightmost preserved site, tweezers are translated to the rightmost unoccupied site by means of a frequency ramp of the radio-frequency

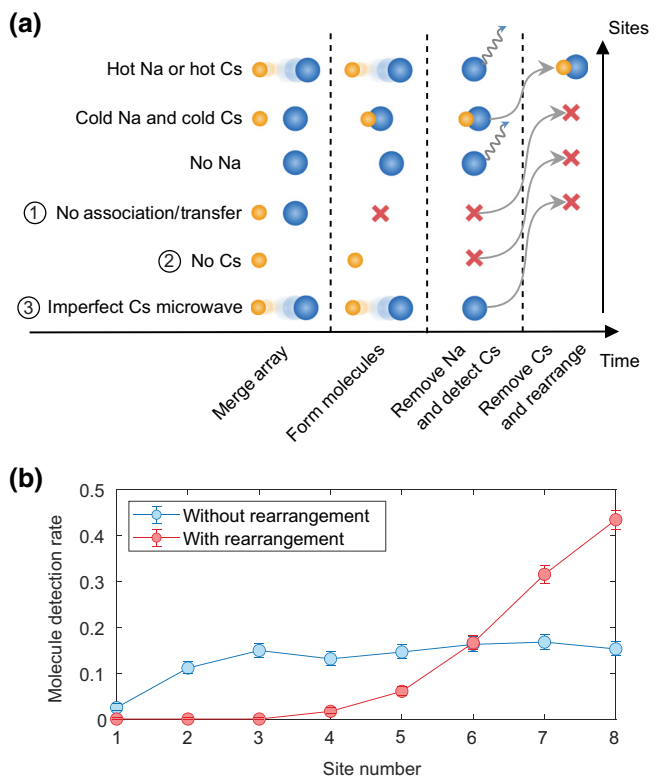


FIG. 3. The rearrangement of molecules based on the detection of Cs atoms at 864 G. (a) The behavior of the rearrangement algorithm for possible occupations of the 1064-nm tweezers for sites at which Na and Cs are both detected before Raman sideband cooling. Sites at which Cs is not detected are rearranged. Such sites may not contain a ground-state molecule if: (1) the molecule does not survive Raman transfer to the ground state, (2) the Cs atom is lost when the Na and Cs arrays are merged, and (3) the Cs transition from $|g'\rangle$ to $|g\rangle$ is not successful. (b) The ground-state molecule population with and without molecular rearrangement that is detected by Cs imaging at high-field.

(rf) tones generating each tweezer. The translation is performed using a minimum-jerk trajectory for the start and end of the ramp, linked by a constant-velocity region. At the same time, the rf amplitudes are ramped to compensate for changes in diffraction efficiency across the bandwidth of the acousto-optic deflector (AOD) generating the tweezers, keeping the tweezer depth approximately constant during the move. The hardware for rearrangement has been described previously for atom rearrangement in our system [56]. Briefly, images from the CCD camera are processed on a control computer to determine which sites to preserve and the information is passed to an arbitrary waveform generator that controls rf frequencies sent to an AOD for the 1064-nm tweezers to implement the aforementioned rearrangement protocol.

The measured ground-state molecule population is shown in Fig. 3(b). On average, we detect 13.2(4)% filling of ground-state molecules without rearrangement. We

note that we rearrange the atomic arrays to the rightmost sites prior to the creation of molecules, resulting in a lower detection rate of molecules on the left side of the array. Accounting for the loss from the detuned Raman process and the false-negative rate of Cs high-field imaging, we estimate a 18.0(9)% filling of the array, which is consistent with the prior estimate. Molecular rearrangement significantly improves molecular density on the right side of the array. We detect a factor-of-2.8(3) improvement in the filling of the rightmost site and the detection rate of a pair of molecules in the two rightmost sites improves from 4.3(8)% to 16(2)%. This represents a fourfold improvement in statistics for observing the dipolar interaction between two particles.

In order to quantify any molecule heating induced by the rearrangement process, we dissociate the molecules, unmerge the 616-nm and 1064-nm tweezers, lower the magnetic field, and measure the temperature of the resulting Cs atoms in the 1064-nm trap using the Raman sideband thermometry method described in detail previously [56,63]. The Cs atom temperature provides an upper bound on the molecule. Using this metric, we detect no resolvable decrease in the motional ground-state population as a result of the rearrangement. Further details of the thermometry and measured atom temperature are provided in Appendix E.

IV. MULTISTATE READOUT

The ability to perform sequential readout of multiple states of a particle is crucial for qudit-based computation or multilevel quantum simulation applications, due to the quadratic scaling of the number of measurements required for full quantum state tomography [64]. Multistate readout via fluorescence imaging has been demonstrated in trapped ion qudits [21,23] and would be highly applicable to molecules due to their abundance of long-lived rotational and hyperfine states [11].

In prior work, we have measured the $|0\rangle \equiv |N=0, m_N=0\rangle$ rotational (N) population by reversing the adiabatic steps used for molecule formation: two-photon transfer to a weakly bound Feshbach state, magnetodissociation, the return of Na atoms into their original tweezer array, and the detection of Na and Cs with fluorescence imaging at 5.5 G. Since neither the Na nor Cs D_2 imaging light induces significant scattering of the molecules, we can instead perform multiple rounds of state-selective molecular dissociation and imaging to detect the population in $|0\rangle$ and $|1\rangle \equiv \frac{1}{\sqrt{2}}(|N=1, m_N=-1\rangle - |N=1, m_N=1\rangle)$, where the rotational quantization axis is defined by the magnetic field. Imaging atoms at high field is advantageous for this application, as it avoids the 150 ms required to ramp the magnetic field down and up between 5.5 and 865 G.

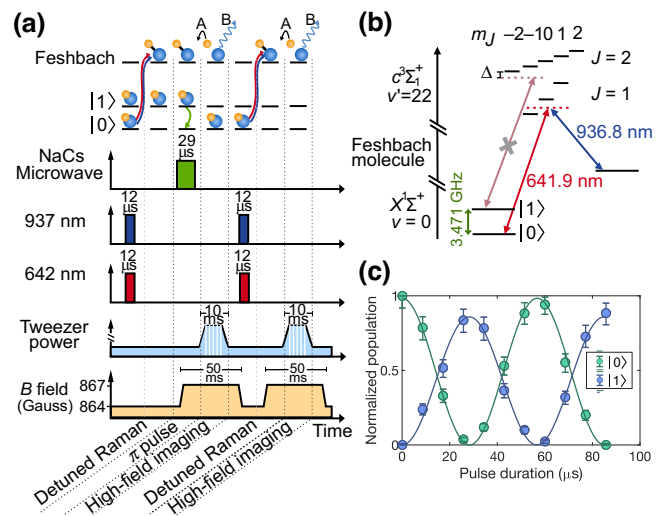


FIG. 4. The sequential detection of multiple rotational states. (a) The timing diagram, showing the sequential dissociation of $|0\rangle$ and $|1\rangle$ and imaging of the resulting Cs atoms. (b) The energy level diagram of NaCs, showing the ground rotational levels, the excited intermediate states used for detuned Raman transfer [55,56], and the weakly bound Feshbach state. The population in $N = 1$ is protected during detuned Raman transfer by a careful choice of single-photon detuning. (c) The multistate detection of the rotational population during driven Rabi oscillations between $|0\rangle$ and $|1\rangle$.

The sequence of field ramps and pulses required for sequential readout of the rotational states $|0\rangle$ and $|1\rangle$ is shown in Fig. 4(a). The total time needed to detect each rotational state is 50 ms. The population in $|0\rangle$ is converted to a weakly bound molecule via detuned Raman transfer. Prior to its detection, a microwave π pulse transfers the population in $|1\rangle$ to $|0\rangle$. The weakly bound molecule is dissociated and the resulting Cs atoms, corresponding to the initial $|0\rangle$ population, are detected. Following imaging, a pulse is used to clean out any remaining Cs atoms from $|g'\rangle$ and $|g\rangle$ before the next imaging step. Subsequently, the remaining population is dissociated and Cs atoms originally from $|1\rangle$ are also detected.

The frequency of the 642-nm Raman laser that connects the ground molecular state to the $c^3\Sigma$ potential is carefully selected to prevent population in the $|1\rangle$ state from scattering during the first transfer of $|0\rangle$ to the Feshbach state. The 642-nm laser can couple $|1\rangle$ to the $J = 1$ and $J = 2$ rotational levels of the excited $v' = 22$ manifold [57], where J denotes the sum of the rotational N and electronic spin S angular momenta of the molecule. We have chosen the frequency of the 642-nm laser to be $h \times 500$ MHz blue detuned from the $|J = 1, m_J = -1\rangle$, such that direct excitation from $|1\rangle$ would fall between the energy of the $J = 1$ and $J = 2$ levels, as shown in Fig. 4(b). The polarization of the two 642-nm and 937-nm Raman beams is therefore set to $\hat{\sigma}^-$ to maximize the Raman Rabi frequency contribution

from the closest detuned $|J = 1, m_J = -1\rangle$ intermediate state.

To demonstrate sequential imaging, we apply a resonant microwave pulse following molecule rearrangement and measure Rabi oscillations between $|0\rangle$ and $|1\rangle$, shown in Fig. 4(c). The error bars represent 68.3% confidence intervals based on the binomial distribution of the measurement outcomes for a given experimental condition. The sequentially detected population is normalized to a parallel measurement of the population in $|0\rangle$ just after molecule formation. To calibrate the imaging fidelity, we perform a single microwave π pulse to prepare $|1\rangle$ and then measure the population, normalizing the result to a detection of $|0\rangle$ without any microwaves applied. With fully optimized microwave transfer and imaging conditions, we measure $100^{+0}_{-9}\%$ of the population in $|1\rangle$ [65], consistent with expected losses of 5.6(8)% due to scattering of the tweezer light during the first imaging step. We note, however, that drifts in the alignment and intensity of the detuned Raman lasers [56] as well as thermally induced fluctuations in the magnetic field produced by our Feshbach coils [66], can cause fluctuations in the relative efficiency of the $|0\rangle$ and $|1\rangle$ state detections away from this optimal scattering-limited value. These drifts can be mitigated with regular fine tuning of the readout parameters and could be eliminated with active stabilization of the Raman beams and feed-forward correction of magnetic field drifts, respectively. The multistate readout procedure provides full-state information on all the molecules in the array, allowing for direct single-shot readout of the diagonal elements of any multiqubit density matrix.

V. SITE-SELECTIVE STATE PREPARATION

Site-resolved control of the quantum state of individual particles is necessary for implementing local qubit operations in quantum gates and to prepare arbitrary initial states in quantum simulators. Toward this goal, local control of fields on the scale of the separation between particles is required. In experiments with neutral atoms in optical tweezers, the conventional approach is to apply a global pulse to drive a transition that is made off resonant for certain sites using some combination of tightly focused ac-Stark-shifting beams [67,68] and manipulation of position-defined subensembles [69]. Recent advances in the trapping of molecules in optical tweezers has extended the technique of local ac Stark shifts to arrays of NaCs [70] and CaF [11] molecules, a natural choice given the large centimeter-scale wavelength of microwaves needed for driving rotational transitions as compared to tweezer micrometer spacings.

A drawback of using a computational basis sensitive to differential ac Stark shifts is that intensity noise will result in decoherence. Intensity noise from the optical tweezer is the dominant noise source for molecules due to their

generally large tensor polarizability. For this reason, we seek to initialize molecules within a computational subspace that is insensitive to differential ac Stark shifts from the optical tweezer. The ellipticity of the 1064-nm tweezer polarization is tuned to realize a “magic” state in each rotational level that is free from anisotropic polarizability [6,71]. The lowest two “magic” states, $|0\rangle$ and $|1\rangle$, form our computational basis, the transition between which offers a 2 order-of-magnitude longer spin echo coherence time than the transition between $|0\rangle$ and a nonmagic state $|1'\rangle \equiv \frac{1}{\sqrt{2}}(|N = 1, m_N = -1\rangle + |N = 1, m_N = 1\rangle)$. Since the computational basis cannot be ac Stark shifted with the 1064-nm tweezer, we make use of the large $h \times 5.55(1)$ MHz/(MW/cm²) differential ac Stark shift between $|0\rangle$ and $|1'\rangle$. The $|0\rangle$ population of certain sites is shelved in $|1'\rangle$, allowing the remaining sites to be excited to $|1\rangle$. Shelving avoids the use of an additional near-resonant ac-Stark-shifting beam, which could introduce unwanted scattering that would limit the molecule lifetime and the state-preparation fidelity.

The scheme for site-selective state preparation is illustrated in Fig. 5(a). The array is divided into a set of target sites, which will be transferred to the $|1\rangle$ state, and shelved sites, which will remain in $|0\rangle$ at the end of the sequence. For the shelving process, the trap depths of the target sites are reduced to 25% of the depth of the shelved sites by ramping down the amplitude of the rf tones generating these tweezers. The site-selective initialization is then achieved with a sequence of three microwave pulses:

- (1) With both sites initially in $|0\rangle$, the shelved sites are selectively transferred to the nonmagic $|1'\rangle$ state using a resonant microwave pulse. Due to the depth difference between the sites, the corresponding transition for the target sites is off resonant.
- (2) With the shelved sites in $|1'\rangle$, the target sites are then transferred to the magic $|1\rangle$ state.
- (3) The shelved sites are then transferred back to $|0\rangle$.

At the end of the sequence, the depths of the target sites are ramped back up. Using this procedure, it is possible to initialize an array of molecules in an arbitrary configuration of states $|0\rangle$ and $|1\rangle$. In Fig. 5(b), we show the resolved microwave transitions to the $|1'\rangle$ state for the shelved and target sites at the depths used for initialization, along with the $|0\rangle$ to $|1\rangle$ transition, which has the same frequency for all sites. The site-selective shelving of some sites in $|1'\rangle$ is shown in Fig. 5(c). After calibrating parameters for the shelving and target pulses, we initialize a four-molecule array into an alternating pattern of $|0\rangle$ and $|1\rangle$. We find that we can prepare the target sites in $|1\rangle$ with an average error rate of $4.9^{+0.7}_{-0.7}\%$ and leave shelved sites in $|0\rangle$ with an error rate of $4.5^{+0.6}_{-0.7}\%$. The error rates are determined by comparing the average population of each subensemble measured in the target state and the incorrect computational basis

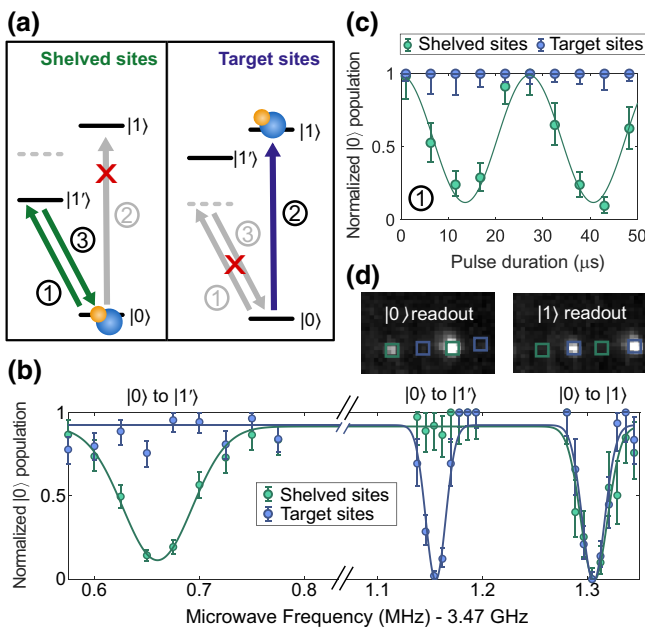


FIG. 5. Site-selective state preparation in a rotational qubit subspace of $|0\rangle$ and $|1\rangle$. (a) The scheme for an array initialized in $|0\rangle$, showing the shelving of more intense traps to an auxiliary nonmagic state $|1'\rangle$ in the $N = 1$ manifold. The remaining target sites are driven to $|1\rangle$ with a global microwave pulse. The shelved sites are then returned to $|0\rangle$ with a final resonant pulse. (b) Microwave spectra showing the resolved transition frequencies from $|0\rangle$ to $|1'\rangle$ for the shelved sites (left) and the target sites (center), as well the magic $|0\rangle$ to $|1\rangle$ transition (right), which has the same frequency for all sites. We note that the three peaks are probed with different microwave powers and pulse times. (c) Step 1 of the site-selective initialization procedure, showing selective transfer of shelved sites to $|1'\rangle$, while target sites remain in $|0\rangle$. (d) Average sequential readout images corresponding to the $|0\rangle$ and $|1\rangle$ population for a site-selective initialization of odd and even sites of the array in $|0\rangle$ and $|1\rangle$, respectively.

state after the initialization sequence. An average fluorescence image showing the array state after site-selective preparation is shown in Fig. 5(d). In the future, these error rates could be lowered with the use of composite passband pulse sequences, which can reduce the sensitivity of a π pulse to small detuning and pulse area errors while suppressing coupling to further off-resonant states [72].

VI. CONCLUSIONS AND OUTLOOK

We have demonstrated several SPAM capabilities for molecules associated from constituent atoms in optical tweezers: nondestructive detection of occupation, rearrangement, site-selective initialization, and sequential multistate detection. Many of these techniques can be generalized to other systems; multistate detection is broadly applicable to bulk and lattice platforms and site-selective initialization can be extended to other multilevel systems in optical tweezers.

Further technical improvements can increase the fidelity of these capabilities. The detuned Raman transfer efficiency—which limits molecule production, the confidence that a rearranged site contains a molecule, and the detection fidelity—can be increased with beam intensity and position stabilization, more laser power, and a narrower intermediate state. Technical progress continues to be made in this area and several species of bialkali molecules have now been transferred to the rovibrational ground state with greater than 90% efficiency [37,73–77]. The false-negative rate of high-field Cs detection can be reduced by improving the transfer fidelity between $|g'\rangle$ and $|g\rangle$ with a stronger microwave Rabi frequency. These improvements, along with further scaling up of the number of initial molecules, would allow the protocol demonstrated here to be used to produce larger completely filled arrays of molecules for quantum information and many-body physics experiments.

The shelving of molecular population in $|1'\rangle$ for site-resolved initialization can be improved with shaped or dynamical decoupling pulses to overcome noise in the transition frequency and off-resonant coupling to other $N = 1$ states. Lastly, molecule loss due to the high tweezer intensity needed for Cs detection may be mitigated by separating and detecting Na atoms in a tweezer the wavelength of which differs from 616 nm, which is destructive to ground-state molecules due to nearby molecular transitions.

In the near term, the SPAM capabilities presented in this work will improve our ability to implement and characterize two-particle gates based on the dipole-dipole exchange interaction. Molecule rearrangement has produced a fourfold increase of our pair-production rate. Additionally, the $|01\rangle$ two-particle state, initialized site selectively, will interact at twice the rate compared to the state initialized by a global $\pi/2$ pulse [10,11]. Single-particle addressability is also a key requirement for realizing a universal gate set with molecules based on the *iSWAP* entangling gate [12]. Sequential multistate imaging will enable faster accumulation of statistics, such as a fourfold reduction in the time required for parity measurements to quantify Bell-state entanglement fidelity, or efficient characterization of errors in precision measurement schemes using molecules [78]. In the long term, advances such as those described here will be necessary to use polar molecules as qudit or n -qubit systems for quantum computation and simulation applications.

ACKNOWLEDGMENTS

We thank Jessie Zhang for early experimental assistance and discussions and Till Rosenband for assistance with Bayesian data analysis. K.-K.N. thanks Cindy Regal for discussions years ago that seeded ideas demonstrated here. This work is supported by Air Force Office of Scientific

TABLE I. Properties of the states relevant to the high-field imaging for Cs, including composition, energy, polarizability, and magnetic field dependence. The state composition and energy relative to the fine-structure energy are specified at 864.1 G in the absence of an external ac electric field. The ground states are best described in the $|F, m_F\rangle$ basis and the excited states are best described in the $|m_I, m_J\rangle$ basis.

State label	State composition	Energy ($\hbar \times \text{GHz}$)	Polarizability ($\frac{\hbar \times \text{MHz}}{\text{MW/cm}^2}$)	Zeeman shift ($\frac{\hbar \times \text{MHz}}{\text{G}}$)
$ g'\rangle$	$-0.997 3,3\rangle + 0.072 4,3\rangle$	-6.139	-51.0	-1.175
$ g\rangle$	$ 4,4\rangle$	5.231	-59.2	1.399
$ g''\rangle$	$-0.997 4,3\rangle - 0.072 3,3\rangle$	4.987	-58.5	1.172
$ g'''\rangle$	$-0.995 4,2\rangle - 0.099 3,2\rangle$	4.731	-57.7	0.926
$ e\rangle$	$ 7/2,3/2\rangle$	2.682	21.8	2.799
$ e'\rangle$	$0.998 5/2,3/2\rangle + 0.067 7/2,1/2\rangle$	2.615	21.7	2.791
$ e''\rangle$	$0.998 7/2,1/2\rangle - 0.067 5/2,3/2\rangle$	0.885	-9.6	0.940
$ e'''\rangle$	$0.997 7/2,-1/2\rangle - 0.075 5/2,1/2\rangle$	-0.906	-13.8	-0.925

Research (AFOSR) Multidisciplinary Research Program of the University Research Initiative (MURI) Grant No. #FA9550-20-1-0323, AFOSR Grant No. #FA9550-23-1-0538, and National Science Foundation (NSF) Grant No. #PHY-2110225.

Note added.—We recently became aware of a concurrent work using RbCs molecules from the Cornish group at Durham University [79].

APPENDIX A: ATOMIC STRUCTURE

The hyperfine structure of the $3^2S_{1/2}$, $3^2P_{3/2}$, $6^2S_{1/2}$, and $6^2P_{3/2}$ fine-structure levels of Na and Cs at the conditions used for molecule formation is provided to complement the discussion of high-field imaging in Sec. II. Atomic parameters are obtained from Ref. [80]. We assume that the atoms experience two external fields: a magnetic field that defines the quantization axis $\vec{B} = 864.1 \text{ G } \hat{z}$, and an optical tweezer specified by ellipticity $\chi = 0.9553$ and orientation $\psi = 0$ with polarization

$$\hat{\epsilon} = e^{-i\psi} \frac{\cos(\chi) - \sin(\chi)}{\sqrt{2}} \hat{\sigma}_- - e^{i\psi} \frac{\cos(\chi) + \sin(\chi)}{\sqrt{2}} \hat{\sigma}_+. \quad (\text{A1})$$

The hyperfine structure is calculated by diagonalizing the bare-hyperfine-structure, Zeeman-shift, and ac-Stark-shift terms in the Hamiltonian in the $|I, J, m_I, m_J\rangle$ basis and assuming no coupling between fine-structure levels. The ac Stark shift is incorporated following the procedure in Ref. [81]. The composition, energy, polarizability, and magnetic dependence of relevant eigenstates are provided in Tables I and II for Cs and Na, respectively.

APPENDIX B: MOLECULAR STRUCTURE

Ground-state molecules are produced in our system via magnetoassociation of atom pairs followed by two-photon detuned Raman transfer. Three molecular potentials are involved in the molecular creation process, illustrated in

the inset of Fig. 1. Initially, pairs of Na and Cs atoms in a single optical tweezer are prepared in the $|g'\rangle_{\text{Cs}} |g'\rangle_{\text{Na}}$ hyperfine channel, which has mixed singlet-triplet character. That is, it can be expressed as a linear combination of states in the singlet ($X^1\Sigma^+$) and triplet ($a^3\Sigma_1^+$) molecular potentials that tend asymptotically to the unbound atom pair at large interatomic separations. We adiabatically transfer from the atom pair to a weakly bound molecular state, also with mixed singlet-triplet character, using magnetoassociation at a Feshbach resonance. For further details of the magnetoassociation, we refer readers to Ref. [43]. The desired endpoint of molecule preparation is the rovibrational ground state of the $X^1\Sigma^+$ potential. In order to bridge the gap between the weakly bound Feshbach state and the rovibrational ground state, we perform a two-photon transfer via the $v' = 22$ state in the electronically excited $c^3\Sigma_1^+$ molecular potential. A detailed discussion of the structure of this intermediate state can be found in Ref. [57]. We transfer to $X^1\Sigma^+$ via this intermediate state using a two-photon detuned Raman process. In this work, we choose to use detuned Raman rather than Stimulated Raman adiabatic passage (STIRAP) for the two-photon transfer, as it allows us to detune from single-photon resonance and minimize excess scattering from the intermediate state. Further discussion of the detuned Raman process and its efficiency can be found in Ref. [56].

APPENDIX C: QUANTIFYING IMAGING FIDELITY

We describe the standard procedure used to determine the fidelity of Cs high-field imaging. Cs atoms are optically cycled on the $|g\rangle$ to $|e\rangle$ transition and fluorescence is detected by a CCD camera via a 0.55-NA objective. Since the fluorescence of an atom is spread across several camera pixels, we sum the photons collected in a 3×3 region of pixels centered on each atom. We observe two distributions in the number of collected counts over many experimental cycles; a lower-count “dark” peak corresponding to

TABLE II. Properties of the states relevant to the high-field imaging for Na, including composition, energy, polarizability, and magnetic field dependence. The state composition and energy relative to the fine-structure energy are specified at 864.1 G in the absence an external ac electric field. All states are best described in the $|m_I, m_J\rangle$ basis.

State label	State composition	Energy ($\hbar \times \text{GHz}$)	Polarizability $\left(\frac{\hbar \times \text{MHz}}{\text{MW/cm}^2}\right)$	Zeeman shift $\left(\frac{\hbar \times \text{MHz}}{\text{G}}\right)$
$ g'\rangle$	$0.977 {-1/2, -1/2}\rangle - 0.215 {3/2, -1/2}\rangle$	-2.046	-11.0	-1.273
$ g\rangle$	$ {3/2, 1/2}\rangle$	1.874	-11.0	1.400
$ g''\rangle$	$-0.977 {3/2, -1/2}\rangle - 0.215 {-1/2, -1/2}\rangle$	1.601	-11.0	1.271
$ g'''\rangle$	$-0.951 {1/2, 1/2}\rangle - 0.310 {-3/2, 1/2}\rangle$	1.279	11.0	1.132
$ e\rangle$	$ {3/2, 3/2}\rangle$	2.461	87.6	2.799
$ e'\rangle$	$1.000 {1/2, 3/2}\rangle + 0.018 {3/2, 1/2}\rangle$	2.434	87.6	2.800
$ e''\rangle$	$1.000 {3/2, 1/2}\rangle - 0.018 {1/2, 3/2}\rangle$	0.818	6.7	0.933
$ e'''\rangle$	$1.000 {3/2, -1/2}\rangle - 0.020 {1/2, 1/2}\rangle$	-0.823	-37.5	-0.935

background noise and a higher-count “bright” peak corresponding to the convolution of background noise and atom fluorescence. The background noise is likely read noise of the camera; we observe no change in the background distribution when the imaging beams are turned off and the “dark” distribution is better modeled by a Gaussian, rather than a Poissonian distribution that is typical for scattered background light.

We proceed to fit two Gaussian distributions to the collected counts and determine a threshold for counts above which we determine that a site contains an atom. The threshold is chosen to minimize the fraction of the “dark” Gaussian distribution that is above the threshold and the fraction of the “bright” distribution that is below the threshold. Once an optimal threshold is chosen, these two fractions represent the false-positive and false-negative rates of detection. The fidelity is then defined as the difference between unity and the sum of these false rates.

APPENDIX D: ERROR ANALYSIS AND NORMALIZATION

The data collected from the experiment consist of a sequence of Bernoulli trials the outcome of which is determined by binary detection of fluorescence imaging, as described in Appendix C. The number of successes (S) and trials (T) provides an estimate probability ($\theta' = S/T$) of the true probability (θ) of ending the experiment with an atom in a given site. Since the data are binomial, uncorrelated, and are sampled from a fixed true probability, we may assign a binomial distribution to the data that represents the probability of obtaining S given θ and T :

$$p(S|\theta, T) = \binom{T}{S} \theta^S (1-\theta)^{T-S}.$$

Several times herein, we compute the ratio of two data points A and B with the methods of Ref. [82], where A is the detected molecule population in the ground rotational state after a sequence of microwave pulses and B is

the detected molecule population in the ground rotational state without applying microwave pulses. The ratio A/B provides the fraction of the population that remains in the ground rotational state. We define the likelihood of measuring A to be $p(S_A|r\theta_B, T)$ and the likelihood of measuring B to be $p(S_B|\theta_B, T)$, where r is an unknown parameter for the sought after ratio and θ_B is an unknown parameter for the detected molecule filling. Since both data points are independent, their joint probability density is the product of their probability densities:

$$\begin{aligned} p(S_A, S_B|r, \theta_B, T) \\ \propto (r\theta_B)^{S_A} (1-r\theta_B)^{T-S_A} (\theta_B)^{S_B} (1-\theta_B)^{T-S_B}. \end{aligned}$$

Our prior knowledge of the independent parameters r and θ_B is that both parameters must be constrained between 0 and 1. The corresponding prior probability is $p(r, \theta_B) = 1$ on the squared unit interval. Using Bayes’ formula, the joint posterior distribution is

$$\begin{aligned} p(r, \theta_B|S_A, S_B, T) \\ \propto (r\theta_B)^{S_A} (1-r\theta_B)^{T-S_A} (\theta_B)^{S_B} (1-\theta_B)^{T-S_B} \end{aligned}$$

for r and θ_B within the unit interval. We then integrate over θ_B to obtain the marginal posterior distribution

$$\begin{aligned} p(r|S_A, S_B, T) &\propto \int_0^1 d\theta_B p(r, \theta_B|S_A, S_B, T) \\ &\propto (r)^{S_A} {}_2\tilde{F}_1(1+S_A, S_B, S_A-T, 2+S_A+T, r), \end{aligned}$$

where ${}_2\tilde{F}_1$ is a regularized hypergeometric function.

The error bars are obtained by choosing the smallest interval of the probability density of the marginal posterior distribution that contains 68.27% of the probability. These error bars differ from confidence intervals in that they are not centered about the mean of the density. This is a standard technique when the underlying distribution is asymmetric, as is the case when $S_A \geq S_B$. The data point is placed on the peak of the probability density, corresponding to the probability of maximum likelihood.

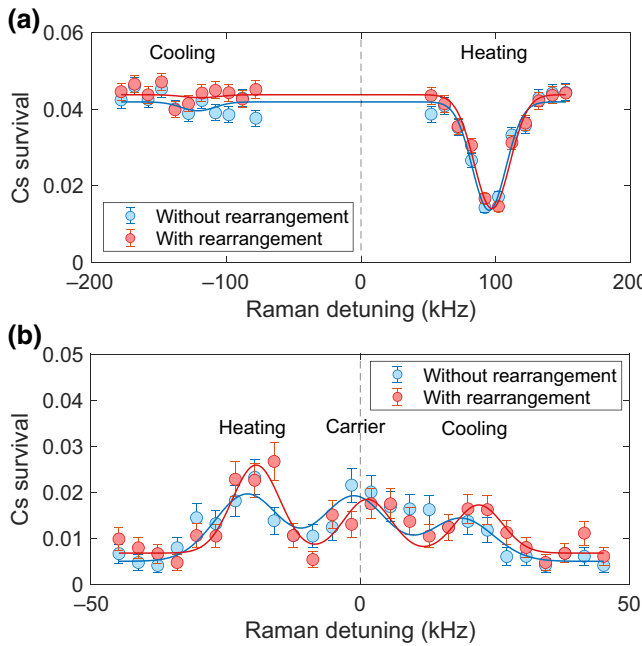


FIG. 6. (a) Radial sideband thermometry on Cs atoms, starting in the $|F = 3, m_F = 3\rangle$ state and attempting to drive to heating and cooling sidebands of the transition to $|F = 4, m_F = 4\rangle$, both with and without the molecule-rearrangement step active. (b) Axial sideband thermometry, starting in $|F = 4, m_F = 4\rangle$ and driving to $|F = 3, m_F = 3\rangle$.

APPENDIX E: PROBING MOLECULE TEMPERATURE

As described in the main text, we probe the motional temperature of the ground-state molecules after rearrangement by first dissociating them and then performing Raman sideband thermometry on the resulting Cs atoms. This method can only provide an upper bound on the temperature of the molecules, as the atoms undergo additional heating following dissociation, most notably during the unmerging of the 1064-nm and 616-nm tweezer arrays. However, atom thermometry can still provide a useful indication of any additional heating induced by the rearrangement process. The thermometry procedure, described in detail previously [56,63,83], involves using a pair of lasers detuned from the Cs D_2 transition to drive motional sidebands on the Raman transition between the $|F = 3, m_F = 3\rangle$ and $|F = 4, m_F = 4\rangle$ hyperfine states. Atoms in $|F = 4, m_F = 4\rangle$ are pushed out with resonant light at the end of the sequence, allowing the population in $|F = 3, m_F = 3\rangle$ to be inferred from the remaining atom survival.

In Fig. 6, we show Raman sideband spectra for the radial and axial axes of the tweezer trap. The weakly confined axial direction corresponds to the tweezer k vector and the radial direction is in the plane of the array. To extract the molecule temperature, we fit the heights of the peaks [83].

In order to constrain the fit, we fix the frequency separation of the peaks based on the measured trap frequencies at the same tweezer depth that we use for Raman sideband cooling. Motion in the radial direction would be particularly deleterious for future work on coherent dipole-dipole interactions, because it corresponds to a linear change in the molecule-molecule separation r . Because of the array geometry, r is only quadratically sensitive to axial relative motion. In the radial direction, we measure motional ground-state fractions of 92(7)% without rearrangement and 97(6)% with rearrangement, which is consistent to within one standard error with there being no radial heating during rearrangement. In the axial direction, we measure 39(20)% ground-state population without rearrangement and 54(17)% with rearrangement, which is also consistent to within one standard error with no heating. Note that for the axial spectrum, we introduce an additional optical pumping pulse to transfer atoms to the $|F = 4, m_F = 4\rangle$ state before taking the spectrum. At the expense of inducing a small amount of heating, this pulse allows us to more easily resolve the spectrum from the background.

- [1] S. Ospelkaus, K.-K. Ni, G. Quéméner, B. Neyenhuis, D. Wang, M. H. G. de Miranda, J. L. Bohn, J. Ye, and D. S. Jin, Controlling the hyperfine state of rovibronic ground-state polar molecules, *Phys. Rev. Lett.* **104**, 030402 (2010).
- [2] J. W. Park, Z. Z. Yan, H. Loh, S. A. Will, and M. W. Zwierlein, Second-scale nuclear spin coherence time of ultracold $^{23}\text{Na}^{40}\text{K}$ molecules, *Science* **357**, 372 (2017).
- [3] P. D. Gregory, J. A. Blackmore, S. L. Bromley, J. M. Hutson, and S. L. Cornish, Robust storage qubits in ultracold polar molecules, *Nat. Phys.* **17**, 1149 (2021).
- [4] J. Lin, J. He, M. Jin, G. Chen, and D. Wang, Secondscale coherence on nuclear spin transitions of ultracold polar molecules in 3D optical lattices, *Phys. Rev. Lett.* **128**, 223201 (2022).
- [5] S. Burchesky, L. Anderegg, Y. Bao, S. S. Yu, E. Chae, W. Ketterle, K.-K. Ni, and J. M. Doyle, Rotational coherence times of polar molecules in optical tweezers, *Phys. Rev. Lett.* **127**, 123202 (2021).
- [6] A. J. Park, L. R. Picard, G. E. Patenotte, J. T. Zhang, T. Rosenband, and K.-K. Ni, Extended rotational coherence of polar molecules in an elliptically polarized trap, *Phys. Rev. Lett.* **131**, 183401 (2023).
- [7] P. D. Gregory, L. M. Fernley, A. L. Tao, S. L. Bromley, J. Stepp, Z. Zhang, S. Kotochigova, K. R. A. Hazzard, and S. L. Cornish, Second-scale rotational coherence and dipolar interactions in a gas of ultracold polar molecules, *Nat. Phys.* **20**, 415 (2024).
- [8] A. V. Gorshkov, S. R. Manmana, G. Chen, J. Ye, E. Demler, M. D. Lukin, and A. M. Rey, Tunable superfluidity and quantum magnetism with ultracold polar molecules, *Phys. Rev. Lett.* **107**, 115301 (2011).
- [9] L. Christakis, J. S. Rosenberg, R. Raj, S. Chi, A. Morningstar, D. A. Huse, Z. Z. Yan, and W. S. Bakr, Probing

- site-resolved correlations in a spin system of ultracold molecules, *Nature* **614**, 64 (2023).
- [10] C. M. Holland, Y. Lu, and L. W. Cheuk, On-demand entanglement of molecules in a reconfigurable optical tweezer array, *Science* **382**, 1143 (2023).
- [11] Y. Bao, S. S. Yu, L. Anderegg, E. Chae, W. Ketterle, K.-K. Ni, and J. M. Doyle, Dipolar spin-exchange and entanglement between molecules in an optical tweezer array, *Science* **382**, 1138 (2023).
- [12] K.-K. Ni, T. Rosenband, and D. D. Grimes, Dipolar exchange quantum logic gate with polar molecules, *Chem. Sci.* **9**, 6830 (2018).
- [13] Y.-X. Liu, L. Zhu, J. Luke, J. J. A. Houwman, M. C. Babin, M.-G. Hu, and K.-K. Ni, Quantum interference and entanglement in ultracold atom-exchange reactions, [arXiv:2310.07620](https://arxiv.org/abs/2310.07620).
- [14] J. J. Hudson, D. M. Kara, I. J. Smallman, B. E. Sauer, M. R. Tarbutt, and E. A. Hinds, Improved measurement of the shape of the electron, *Nature* **473**, 493 (2011).
- [15] T. S. Roussy, L. Caldwell, T. Wright, W. B. Cairncross, Y. Shagam, K. B. Ng, N. Schlossberger, S. Y. Park, A. Wang, J. Ye, and E. A. Cornell, An improved bound on the electron's electric dipole moment, *Science* **381**, 46 (2023).
- [16] V. Andreev, D. G. Ang, D. DeMille, J. M. Doyle, G. Gabrielse, J. Haefner, N. R. Hutzler, Z. Lasner, C. Meisenhelder, B. R. O'Leary, C. D. Panda, A. D. West, E. P. West, and X. Wu, Improved limit on the electric dipole moment of the electron, *Nature* **562**, 355 (2018).
- [17] D. Barredo, S. de Léséleuc, V. Lienhard, T. Lahaye, and A. Browaeys, An atom-by-atom assembler of defect-free arbitrary two-dimensional atomic arrays, *Science* **354**, 1021 (2016).
- [18] M. Endres, H. Bernien, A. Keesling, H. Levine, E. R. Anschuetz, A. Krajenbrink, C. Senko, V. Vuletic, M. Greiner, and M. D. Lukin, Atom-by-atom assembly of defect-free one-dimensional cold atom arrays, *Science* **354**, 1024 (2016).
- [19] A. L. Shaw, P. Scholl, R. Finkelstein, I. S. Madjarov, B. Grinkemeyer, and M. Endres, Dark-state enhanced loading of an optical tweezer array, *Phys. Rev. Lett.* **130**, 193402 (2023).
- [20] M. Martinez-Dorantes, W. Alt, J. Gallego, S. Ghosh, L. Ratschbacher, and D. Meschede, State-dependent fluorescence of neutral atoms in optical potentials, *Phys. Rev. A* **97**, 023410 (2018).
- [21] P. J. Low, B. White, and C. Senko, Control and readout of a 13-level trapped ion qudit, [arXiv:2306.03340](https://arxiv.org/abs/2306.03340).
- [22] G. Semeghini, H. Levine, A. Keesling, S. Ebadi, T. T. Wang, D. Bluvstein, R. Verresen, H. Pichler, M. Kalinowski, R. Samajdar, A. Omran, S. Sachdev, A. Vishwanath, M. Greiner, V. Vuletić, and M. D. Lukin, Probing topological spin liquids on a programmable quantum simulator, *Science* **374**, 1242 (2021).
- [23] M. Ringbauer, M. Meth, L. Postler, R. Stricker, R. Blatt, P. Schindler, and T. Monz, A universal qudit quantum processor with trapped ions, *Nat. Phys.* **18**, 1053 (2022).
- [24] P. Scholl, A. L. Shaw, R. B.-S. Tsai, R. Finkelstein, J. Choi, and M. Endres, Erasure conversion in a high-fidelity Rydberg quantum simulator, *Nature* **622**, 273 (2023).
- [25] D. Bluvstein, *et al.*, Logical quantum processor based on reconfigurable atom arrays, *Nature* **624**, 1 (2023).
- [26] M. D. D. Rosa, Laser-cooling molecules—concept, candidates, and supporting hyperfine-resolved measurements of rotational lines in the A-X(0,0) band of CaH), *Eur. Phys. J. D* **31**, 395 (2004).
- [27] M. R. Tarbutt, Laser cooling of molecules, *Contemp. Phys.* **59**, 356 (2018).
- [28] E. S. Shuman, J. F. Barry, and D. DeMille, Laser cooling of a diatomic molecule, *Nature* **467**, 820 (2010).
- [29] S. Truppe, H. J. Williams, M. Hambach, L. Caldwell, N. J. Fitch, E. A. Hinds, B. E. Sauer, and M. R. Tarbutt, Molecules cooled below the Doppler limit, *Nat. Phys.* **13**, 1173 (2017).
- [30] L. Anderegg, L. W. Cheuk, Y. Bao, S. Burchesky, W. Ketterle, K.-K. Ni, and J. M. Doyle, An optical tweezer array of ultracold molecules, *Science* **365**, 1156 (2019).
- [31] Y. Wu, J. J. Burau, K. Mehling, J. Ye, and S. Ding, High phase-space density of laser-cooled molecules in an optical lattice, *Phys. Rev. Lett.* **127**, 263201 (2021).
- [32] N. B. Vilas, P. Robichaud, C. Hallas, G. K. Li, L. Anderegg, and J. M. Doyle, An optical tweezer array of ultracold polyatomic molecules, [arXiv:2311.07529](https://arxiv.org/abs/2311.07529).
- [33] T. Kohler, K. Goral, and P. S. Julienne, Production of cold molecules via magnetically tunable Feshbach resonances, *Rev. Mod. Phys.* **78**, eid 1311 (2006).
- [34] J. G. Danzl, E. Haller, M. Gustavsson, M. J. Mark, R. Hart, N. Bouloufa, O. Dulieu, H. Ritsch, and H.-C. Nägerl, Quantum gas of deeply bound ground state molecules, *Science* **321**, 1062 (2008).
- [35] K.-K. Ni, S. Ospelkaus, M. H. G. de Miranda, A. Pe'er, B. Neyenhuis, J. J. Zirbel, S. Kotochigova, P. S. Julienne, D. S. Jin, and J. Ye, A high phase-space-density gas of polar molecules, *Science* **322**, 231 (2008).
- [36] F. Lang, K. Winkler, C. Strauss, R. Grimm, and J. Hecker Denschlag, Ultracold triplet molecules in the rovibrational ground state, *Phys. Rev. Lett.* **101**, 133005 (2008).
- [37] T. Takekoshi, L. Reichsöllner, A. Schindewolf, J. M. Hutson, C. R. Le Sueur, O. Dulieu, F. Ferlaino, R. Grimm, and H.-C. Nägerl, Ultracold dense samples of dipolar RbCs molecules in the rovibrational and hyperfine ground state, *Phys. Rev. Lett.* **113**, 205301 (2014).
- [38] P. K. Molony, P. D. Gregory, Z. Ji, B. Lu, M. P. Köppinger, C. R. Le Sueur, C. L. Blackley, J. M. Hutson, and S. L. Cornish, Creation of ultracold $^{87}\text{Rb}^{133}\text{Cs}$ molecules in the rovibrational ground state, *Phys. Rev. Lett.* **113**, 255301 (2014).
- [39] J. W. Park, S. A. Will, and M. W. Zwierlein, Ultracold dipolar gas of fermionic $^{23}\text{Na}^{40}\text{K}$ molecules in their absolute ground state, *Phys. Rev. Lett.* **114**, 205302 (2015).
- [40] M. Guo, B. Zhu, B. Lu, X. Ye, F. Wang, R. Vexiau, N. Bouloufa-Maafa, G. Quéméner, O. Dulieu, and D. Wang, Creation of an ultracold gas of ground-state dipolar $^{23}\text{Na}^{87}\text{Rb}$ molecules, *Phys. Rev. Lett.* **116**, 205303 (2016).
- [41] X. He, K. Wang, J. Zhuang, P. Xu, X. Gao, R. Guo, C. Sheng, M. Liu, J. Wang, J. Li, G. V. Shlyapnikov, and M. Zhan, Coherently forming a single molecule in an optical trap, *Science* **370**, 331 (2020).
- [42] K. K. Voges, P. Gersema, M. Meyer zum Alten Borgloh, T. A. Schulze, T. Hartmann, A. Zenesini, and S. Ospelkaus,

- Ultracold gas of bosonic $^{23}\text{Na}^{39}\text{K}$ ground-state molecules, *Phys. Rev. Lett.* **125**, 083401 (2020).
- [43] J. T. Zhang, Y. Yu, W. B. Cairncross, K. Wang, L. R. B. Picard, J. D. Hood, Y.-W. Lin, J. M. Hutson, and K.-K. Ni, Forming a single molecule by magnetoassociation in an optical tweezer, *Phys. Rev. Lett.* **124**, 253401 (2020).
- [44] Y. Yu, K. Wang, J. D. Hood, L. R. B. Picard, J. T. Zhang, W. B. Cairncross, J. M. Hutson, R. Gonzalez-Ferez, T. Rosenband, and K.-K. Ni, Coherent optical creation of a single molecule, *Phys. Rev. X* **11**, 031061 (2021).
- [45] D. K. Ruttle, A. Guttridge, S. Spence, R. C. Bird, C. R. Le Sueur, J. M. Hutson, and S. L. Cornish, Formation of ultracold molecules by merging optical tweezers, *Phys. Rev. Lett.* **130**, 223401 (2023).
- [46] L. Homeier, T. J. Harris, T. Blatz, U. Schollwöck, F. Grusdt, and A. Bohrdt, Antiferromagnetic bosonic t_j models and their quantum simulation in tweezer arrays, [arXiv:2305.02322](https://arxiv.org/abs/2305.02322).
- [47] R. Sawant, J. A. Blackmore, P. D. Gregory, J. Mur-Petit, D. Jaksch, J. Aldegunde, J. M. Hutson, M. R. Tarbutt, and S. L. Cornish, Ultracold polar molecules as qudits, *New J. Phys.* **22**, 013027 (2020).
- [48] F. Wolf, Y. Wan, J. C. Heip, F. Gebert, C. Shi, and P. O. Schmidt, Non-destructive state detection for quantum logic spectroscopy of molecular ions, *Nature* **530**, 457 (2016).
- [49] C.-W. Chou, C. Kurz, D. B. Hume, P. N. Plessow, D. R. Leibrandt, and D. Leibfried, Preparation and coherent manipulation of pure quantum states of a single molecular ion, *Nature* **545**, 203 (2017).
- [50] A. Jamadagni, S. Ospelkaus, L. Santos, and H. Weimer, Quantum Zeno-based detection and state engineering of ultracold polar molecules, *Phys. Rev. Res.* **3**, 033208 (2021).
- [51] Q. Guan, M. Highman, E. J. Meier, G. R. Williams, V. Scarola, B. DeMarco, S. Kotochigova, and B. Gadway, Nondestructive dispersive imaging of rotationally excited ultracold molecules, *Phys. Chem. Chem. Phys.* **22**, 20531 (2020).
- [52] W. C. Campbell and E. R. Hudson, Dipole-phonon quantum logic with trapped polar molecular ions, *Phys. Rev. Lett.* **125**, 120501 (2020).
- [53] K. Wang, C. P. Williams, L. R. Picard, N. Y. Yao, and K.-K. Ni, Enriching the quantum toolbox of ultracold molecules with Rydberg atoms, *PRX Quantum* **3**, 030339 (2022).
- [54] C. Zhang and M. Tarbutt, Quantum computation in a hybrid array of molecules and Rydberg atoms, *PRX Quantum* **3**, 030340 (2022).
- [55] W. B. Cairncross, J. T. Zhang, L. R. B. Picard, Y. Yu, K. Wang, and K.-K. Ni, Assembly of a rovibrational ground state molecule in an optical tweezer, *Phys. Rev. Lett.* **126**, 123402 (2021).
- [56] J. T. Zhang, L. R. B. Picard, W. B. Cairncross, K. Wang, Y. Yu, F. Fang, and K.-K. Ni, An optical tweezer array of ground-state polar molecules, *Quantum Sci. Technol.* **7**, 035006 (2022).
- [57] L. R. B. Picard, J. T. Zhang, W. B. Cairncross, K. Wang, G. E. Patenotte, A. J. Park, Y. Yu, L. R. Liu, J. D. Hood, R. González-Férez, and K.-K. Ni, High resolution photoassociation spectroscopy of the excited $c^3\Sigma_1^+$ potential of $^{23}\text{Na}^{133}\text{Cs}$, *Phys. Rev. Res.* **5**, 023149 (2023).
- [58] B. Nikolov, E. Diamond-Hitchcock, J. Bass, N. L. R. Spong, and J. D. Pritchard, Randomized benchmarking using nondestructive readout in a two-dimensional atom array, *Phys. Rev. Lett.* **131**, 030602 (2023).
- [59] M. N. H. Chow, B. J. Little, and Y.-Y. Jau, High-fidelity low-loss state detection of alkali-metal atoms in optical tweezer traps, *Phys. Rev. A* **108**, 032407 (2023).
- [60] C. Ospelkaus, S. Ospelkaus, L. Humbert, P. Ernst, K. Sengstock, and K. Bongs, Ultracold heteronuclear molecules in a 3D optical lattice, *Phys. Rev. Lett.* **97**, eid 120402 (2006).
- [61] N. R. Hutzler, L. R. Liu, Y. Yu, and K.-K. Ni, Eliminating light shifts for single atom trapping, *New J. Phys.* **19**, 023007 (2017).
- [62] K. Li, D. C. Spierings, and A. M. Steinberg, Efficient adiabatic rapid passage in the presence of noise, *Phys. Rev. A* **108**, 012615 (2023).
- [63] L. Liu, J. Hood, Y. Yu, J. Zhang, K. Wang, Y.-W. Lin, T. Rosenband, and K.-K. Ni, Molecular assembly of ground-state cooled single atoms, *Phys. Rev. X* **9**, 021039 (2019).
- [64] X. Ma, T. Jackson, H. Zhou, J. Chen, D. Lu, M. D. Mazurek, K. A. G. Fisher, X. Peng, D. Kribs, K. J. Resch, Z. Ji, B. Zeng, and R. Laflamme, Pure-state tomography with the expectation value of Pauli operators, *Phys. Rev. A* **93**, 032140 (2016).
- [65] This represents a maximum likelihood estimate with an asymmetric 68.3% confidence interval determined by the underlying analytic probability distribution following normalization. For further details of the normalization procedure, see Appendix D.
- [66] M. Borkowski, L. Reichsöllner, P. Thekkeppatt, V. Barbé, T. van Roon, K. van Druten, and F. Schreck, Active stabilization of kilogauss magnetic fields to the ppm level for magnetoassociation on ultranarrow Feshbach resonances, *Rev. Sci. Instrum.* **94**, 073202 (2023).
- [67] H. Labuhn, S. Ravets, D. Barredo, L. Béguin, F. Nogrette, T. Lahaye, and A. Browaeys, Single-atom addressing in microtraps for quantum-state engineering using Rydberg atoms, *Phys. Rev. A* **90**, 023415 (2014).
- [68] T. Xia, M. Lichtman, K. Maller, A. W. Carr, M. J. Piotrowicz, L. Isenhower, and M. Saffman, Randomized benchmarking of single-qubit gates in a 2D array of neutral-atom qubits, *Phys. Rev. Lett.* **114**, 100503 (2015).
- [69] D. Bluvstein, H. Levine, G. Semeghini, T. T. Wang, S. Ebadi, M. Kalinowski, A. Keesling, N. Maskara, H. Pichler, M. Greiner, V. Vuletić, and M. D. Lukin, A quantum processor based on coherent transport of entangled atom arrays, *Nature* **604**, 451 (2022).
- [70] K.-K. Ni, in *Bulletin of the American Physical Society* (American Physical Society, Orlando, Florida, 2022), Vol. 67(7). <https://meetings.aps.org/Meeting/DAMOP22/Session/K02.2>.
- [71] T. Rosenband, D. D. Grimes, and K.-K. Ni, Elliptical polarization for molecular Stark shift compensation in deep optical traps, *Opt. Express* **26**, 19821 (2018).
- [72] S. S. Ivanov and N. V. Vitanov, Composite two-qubit gates, *Phys. Rev. A* **92**, 022333 (2015).
- [73] R. Bause, A. Kamijo, X.-Y. Chen, M. Duda, A. Schindewolf, I. Bloch, and X.-Y. Luo, Efficient conversion of closed-channel-dominated Feshbach molecules of $^{23}\text{Na}^{40}\text{K}$

- to their absolute ground state, [Phys. Rev. A](#) **104**, 043321 (2021).
- [74] P. K. Molony, P. D. Gregory, A. Kumar, C. R. LeSueur, J. M. Hutson, and S. L. Cornish, Production of ultracold $^{87}\text{Rb}^{133}\text{Cs}$ in the absolute ground state: Complete characterisation of the stimulated Raman adiabatic passage transfer, [ChemPhysChem](#) **17**, 3811 (2016).
- [75] S. A. Moses, J. P. Covey, M. T. Miecnikowski, B. Yan, B. Gadway, J. Ye, and D. S. Jin, Creation of a low-entropy quantum gas of polar molecules in an optical lattice, [Science](#) **350**, 659 (2015).
- [76] M. Guo, R. Vexiau, B. Zhu, B. Lu, N. Bouloufa-Maafa, O. Dulieu, and D. Wang, High-resolution molecular spectroscopy for producing ultracold absolute-ground-state $^{23}\text{Na}^{87}\text{Rb}$ molecules, [Phys. Rev. A](#) **96**, 052505 (2017).
- [77] C. He, X. Nie, V. Avalos, S. Botsis, S. Kumar, A. Yang, and K. Dieckmann, Efficient creation of ultracold ground state $^6\text{Li}^{40}\text{K}$ polar molecules, [arXiv:2310.03300](#).
- [78] T. Fleig and D. DeMille, Theoretical aspects of radium-containing molecules amenable to assembly from laser-cooled atoms for new physics searches, [New J. Phys.](#) **23**, 113039 (2021).
- [79] D. K. Ruttle, A. Guttridge, T. R. Hepworth, and S. L. Cornish, Enhanced quantum control of individual ultracold molecules using optical tweezer arrays, [PRX Quantum](#) **5**, 020333 (2024).
- [80] N. Šibalić, J. Pritchard, C. Adams, and K. Weatherill, ARC: An open-source library for calculating properties of alkali Rydberg atoms, [Comput. Phys. Commun.](#) **220**, 319 (2017).
- [81] F. L. Kien, P. Schneeweiss, and A. Rauschenbeutel, Dynamical polarizability of atoms in arbitrary light fields: General theory and application to cesium, [Eur. Phys. J. D](#) **67**, 92 (2013).
- [82] R. Little, The statistical analysis of low-level radioactivity in the presence of background counts, [Health Phys.](#) **43**, 693 (1981).
- [83] Y. Yu, N. R. Hutzler, J. T. Zhang, L. R. Liu, J. D. Hood, T. Rosenband, and K.-K. Ni, Motional-ground-state cooling outside the Lamb-Dicke regime, [Phys. Rev. A](#) **97**, 063423 (2018).